1998

Sr- and Ni-Doped $LaCoO_3$ and $LaFeO_3$ Perovskites: New Cathode Materials for Solid-Oxide Fuel Cells

Kevin Huang
University of South Carolina - Columbia, huang46@cec.sc.edu

Hee Y. Lee

John B. Goodenough

Publication Info

Published in *Journal of The Electrochemical Society*, Volume 145, Issue 9, 1998, pages 3220-3227.

Publisher's Version: http://dx.doi.org/10.1149/1.1838789
Huang, K., Lee, H. Y., & Goodenough, J. B. (1998). Sr- and Ni-Doped $LaCoO_3$ and $LaFeO_3$ Perovskites: New Cathode Materials for Solid-Oxide Fuel Cells. Journal of The Electrochemical Society, 145 (9), 3320 - 3227. http://dx.doi.org/10.1149/1.1838789

Sr- and Ni-Doped $LaCoO_3$ and $LaFeO_3$ Perovskites

New Cathode Materials for Solid-Oxide Fuel Cells

Keqin Huang,* Hee Y. Lee, and John B. Goodenough

Texas Materials Institute, The University of Texas at Austin, Austin, Texas 78712, USA

ABSTRACT

An improved cathode material for a solid-oxide fuel cell would be a mixed electronic and oxide-ion conductor with a good catalytic activity for oxygen reduction at an operating temperature $T_{op} \geq 700°C$ and a thermal expansion matched to that of the electrolyte and interconnect. We report on the properties of Sr- and Ni-doped $LaCoO_3$ and $LaFeO_3$ perovskites that meet these criteria. Single-phase regions were determined by X-ray diffraction, and thermogravimetric analysis measurements were used to obtain the temperatures above which oxygen loss, and hence oxide-ion conductivity, occurs. The conductivity and Seebeck measurements indicate the coexistence of both p-type and n-type polaronic charge carriers resulting from an overlap of the Ni^{III}/Ni^{2+} redox couple with the low-spin/intermediate-spin Co^{IV}/Co^{iii} and high-spin Fe^{4+}/Fe^{3+} redox couples. Motional enthalpies $\Delta H_m = 0.03$, 0.02, and 0.08 eV, respectively, were estimated for Ni^{2+}, Co^{IV}, and Fe^{4+} polarons. Optimal compositions have percolation pathways between dopants. Comparisons with transport data for the conventional cathode materials $La_{1-x}Sr_xCoO_{3-\delta}$ and $La_{1-x}Sr_x MnO_3$ indicate superior cathode performance can be expected.

Introduction

The cathode of a solid-oxide fuel cell (SOFC) must perform three functions: (*i*) provide a mechanism for breaking the covalent bond of the O_2 oxidant molecule, (*ii*) accept electrons from the external circuit and distribute them to the reaction sites for the reduction of the oxidant, and (*iii*) allow passage of the reduced O^{2-} ions to the electrolyte for transfer to the anode where they combine with the fuel to form H_2O and CO_2 with the release of electrons to the external circuit. These three functions can be realized in a transition-metal oxide that is both an electronic and an oxide-ion conductor at the operating temperature $T_{op} \geq 700°C$ of the fuel cell.

Numerous transition-metal oxides are metallic, but few of them are also good oxide-ion conductors in the oxidizing atmosphere at the cathode of an SOFC. Any oxide that remains electronically conducting in an O_2 atmosphere can perform the first two functions. At T_{op}, the loss of bound water from the surface of an oxide creates surface-oxygen vacancies, which we denote by $\square_s$. If the oxide is an electronic conductor, the covalent bond of the dioxygen molecule may be broken by the reactions

$$O_2 + \square_s + 2e^- = (O_2)_s^{2-} \quad [1]$$

$$(O_2)_s^{2-} + \square_s + 2e^- = 2\ O_s^{2-} \quad [2]$$

However, unless the surface oxygen contacts an interconnected oxide-ion subarray that also contains oxygen vacancies, conduction of O^{2-} ions across the electrode to the electrolyte is blocked. A representative electronic conductor that is not an oxide-ion conductor is the Sr-doped perovskite $La_{1-x}Sr_xMnO_3$ that has been used extensively as a cathode in ZrO_2-based SOFCs.[1-4] It remains a good electronic conductor, but the lack of oxide-ion vacancies, and hence of oxide-ion conduction, at T_{op} forces the use of thick, porous electrodes containing an extensive array of triple-phase boundaries where gas, electrolyte, and electrode meet. The performance of such a cathode depends sensitively on its microstructure, which may change under operating conditions. Depending on the microstructure, cathode overpotentials have been reported to vary from a few tens to a few hundreds of millivolts. On the other hand, the perovskite system $La_{1-x}Sr_xCoO_{3-\delta}$ contains oxide-ion vacancies in the bulk even in an oxidizing atmosphere; this mixed electronic and oxide-ion conductor has been demonstrated to give an excellent cathode performance with very low overpotential even at high current densities when present as a film on the electrolyte.[5-7]

Unfortunately, the thermal expansion of the $La_{1-x}Sr_xCoO_{3-\delta}$ system is exceptionally high as a result of oxygen loss and a smooth change with increasing temperature from itinerant to polaronic conduction and/or a low-spin to high-spin transition at Co^{III} ions even where an intermediate-spin state has been stabilized over most of the $CoO_{3-\delta}$ matrix.[8] The thermal-expansion mismatch between the electrode and the electrolyte and interconnect makes this system unsuitable as a cathode material for an SOFC subject to repeated thermal cycling. In this paper we report exploration of other mixed-valent perovskite systems that are designed to have a thermal expansion better matched to that of the electrolyte and interconnect and also to be good mixed electronic and oxide-ion conductors in an oxidizing atmosphere at $700 \leq T_{op} \leq 1000°C$. For this purpose, we have used the Ni^{III}/Ni^{2+} redox couple in association with the Fe^{4+}/Fe^{3+} and the low-spin/intermediate-spin Co^{IV}/Co^{iii} couples in the perovskite structure. It was anticipated that the presence of the Ni^{III}/Ni^{2+} redox couple would suppress low-spin-to-high-spin and/or itinerant-to-polaronic transitions so as to reduce the thermal expansion without loss of electrical conductivity.

The early observations of metallic conductivity in the Na_xWO_3, $La_{1-\delta}Mn_{1-\delta}O_3$, and $La_{1-x}Sr_xMnO_3$ mixed-valent perovskite systems became clarified with the prediction by Goodenough and demonstration by Raccah of the metallic conductivity and Pauli paramagnetism of stoichiometric $LaNiO_3$ containing low-spin Ni^{III}.[9] The metallic conductivity is due to strong Ni^{III}–O covalent bonding, which causes the σ-bonding e orbitals of octahedral-site, low-spin Ni^{III}:$t_2^6e^1$ to be transformed into itinerant σ^*-band states as a result of (180°-ϕ) Ni–O–Ni interactions in the NiO_3 array. Subsequently, the systems $La_{1-x}M_xNiO_3$, M = Ca, Sr, and Ba, $0 \leq x \leq 0.05$, were studied extensively by several groups.[10-13] However, these nickelates are thermally unstable at temperatures $T \leq 1100°C$ where they lose oxygen to form Ruddlesden–Popper intergrowth structures $(La,Sr)_{n+1}Ni_nO_{3n+1}$. Below 1100°C, the Ni^{III} ions retain their low-spin configuration, and $LaNiO_3$ has a relatively small thermal-expansion coefficient of $10.0 \times 10^{-6}\ K^{-1}$.

By contrast, the low-spin Co^{III}: $t_2^6e^0$ configuration makes $LaCoO_3$ a diamagnetic insulator at the lowest temperatures; but it becomes more metallic at the highest temperature where an intermediate-spin state $t_2^{5-\delta}\sigma^{*1+\delta}$ is stabilized at the Co^{iii} ions.[14,15] In the system $La_{1-x}Sr_xCoO_{3-\delta}$, the intermediate-spin state Co^{iii} becomes stabilized at lower temperatures,[8,16] but only as a ferromagnetic second phase coexisting with a Co^{III}-rich paramagnetic phase that undergoes a low-spin to high-spin transition. In addition, the larger Sr^{2+} ion may induce a change from itinerant to polaronic behavior above the Curie temperature in the fer-

* Electrochemical Society Student Member.

romagnetic phase. These electronic transitions give $La_{1-x}Sr_xCoO_{3-\delta}$ a large thermal expansion coefficient (TEC $\approx$ 22.0×10^{-6} K^{-1}), but the stability of the Co^{IV}/Co^{III} couple makes it difficult to oxidize fully the $CoO_{3-\delta}$ array and therefore introduces oxygen vacancies into this array while retaining itinerant σ^*-band states in the ferromagnetic phase.[16] Substitution of Ni^{III} for Co^{III} in $La_{1-x}Sr_xCoO_{3-\delta}$ is designed to retain mixed-valent polaronic conduction at temperatures $T > 300$ K while eliminating the Co^{III}-rich phase and with it the low-spin to higher-spin transitions that contribute to the large TEC in $La_{1-x}Sr_xCoO_{3-\delta}$. At the same time, operation on the Co^{IV}/Co^{III} and/or Ni^{III}/Ni^{2+} redox couples should retain oxygen vacancies on the $Co_{1-y}Ni_yO_{3-\delta}$ array.

Undoped $LaFeO_3$ contains high-spin Fe^{3+}:$t_2^3e^2$ localized-electron configurations; it is an antiferromagnetic insulator with a Néel temperature T_N = 750 K.[17,18] In the $La_{1-x}Sr_xFeO_3$ system, a thermally activated hopping of small polarons between Fe ions appears to describe the transport properties. Abbate et al.[19] have shown, with soft X-ray absorption spectroscopy, that the initial substitution of Sr^{2+} for La^{3+} in $La_{1-x}Sr_xFeO_3$ oxidizes primarily the oxygen rather than the iron atoms of the FeO_3 array; the holes occupy molecular antibonding states of an FeO_6 complex in which the dominant component of the ground state is $3d^5\underline{L}$, where $\underline{L}$ denotes a ligand hole. However, as the Sr^{2+}-ion concentration increases, the spectral weight shifts to an increasing Fe-3d component in the hole ground state. The end member $SrFeO_3$ retains a high-spin configuration: the t^3 manifold remains localized, but the single e electron per Fe^{IV} occupies a narrow itinerant-electron band of e-orbital parentage having a large O-2p component. At higher values of x, oxygen is lost at an operating temperature $T_{op} \approx 700$°C, even in an O_2 atmosphere. With retention of high-spin cations, and for $0 < x < 1$, polaronic conduction below the Néel temperature T_N, the oxygen loss does not increase significantly the TEC $\approx$ 12.0 to 13.0 $\times$ 10^{-6} K^{-1}. Moreover, Falcón[20] and Carboni et al.[21] have reported a good catalytic activity for peroxide decomposition and oxygen reduction over the perovskite system $LaFe_{1-y}Ni_yO_3$. Since the Fe ions remain in their high-spin state and the Ni ions in their low-spin state, we can expect the system $La_{1-x}Sr_xFe_{1-y}Ni_yO_{3-\delta}$ will have a TEC typical of a perovskite oxide. In addition, since the Fe^{4+}/Fe^{3+} redox energy lies between the two weakly separated Ni^{III}/Ni^{2+} and Ni^{IV}/Ni^{III} redox energies at the nickel ions, the system can be expected to yield a high polaronic conductivity.

In this paper we report a study of the La–Sr–Co–Ni–O and La–Sr–Fe–Ni–O perovskite systems from synthesis to crystal structure, thermal analysis, electrical conductivity, thermoelectric power, and impedance spectroscopy.

Experimental

Sample preparation.—$La_{1-x}Sr_xCo_{1-y}Ni_yO_3$ (LSCN) compounds were made with the well-known liquid-mixing method.[22] For yielding 5 g of final product, the required stoichiometric amounts of $La(NO_3)_3 \cdot 6H_2O$ (>99.9%), $Sr(NO_3)_2$ (>99%), $Co(NO_3)_2 \cdot 6H_2O$ (>99.9%), $Ni(NO_3)_2 \cdot 6H_2O$ (>99.9%), and citric acid (>99.5%) were dissolved into 200 mL water; then 25 mL ethylene glycol was added under stirring. The mixture was next slowly heated to about 80°C on a thermal plate to allow evaporation of the solvent and the occurrence of the chelating reaction. Since Ni^{III} is wanted in these compounds in order to avoid formation of the unwanted impurity La_2NiO_4, the resulting resins were calcined in an atmosphere of pure O_2 at 750°C overnight. The powders so obtained were then mixed with an equal weight of Na_2CO_3 flux and reacted at 850°C for 10–72 h in air. The mixtures were ballmilled, washed with deionized water several times, and dried in an oven; the resulting fine black powders were pressed into pellets under 200 MPa and finally sintered at 1150 to 1250°C overnight, depending upon the composition. The purpose of using Na_2CO_3 flux was to enhance the diffusion of Ni at lower temperatures. In fact, synthesis without using Na_2CO_3 flux also turned out to yield a single perovskite phase. All the measurements were made on samples synthesized without a flux.

$La_{1-x}Sr_xFe_{1-y}Ni_yO_{3-\delta}$ (LSFN) compounds were synthesized by conventional solid-state reaction. The required amounts of La_2O_3 (>99.99%, after firing at 1000°C more than 3 h), $SrCO_3$ (>99.9%), Co_3O_4 (>99.5%), and NiO (>99.9%) powders were intimately mixed in an agate mortar with the aid of acetone. Pellets were then pressed under 200 MPa and calcined at 1200°C overnight. The partially sintered pellets were reground and calcined again. This process is usually repeated twice until the primary impurity, La_2NiO_4, was totally removed from the main phase. After final regrinding, the powders were further ballmilled into around 1 μm size and pressed into pellets followed by sintering at 1400°C overnight.

Crystal structure.—The crystal structure was determined by powder X-ray diffraction with a Philips PW1729 diffractometer and Cu Kα radiation; a Ni filter was used for all measurements. The scanning angles ranged from 10 to 80° with a step of 2°/min. Silicon powder was used for the internal standard in order to subtract the equipment errors from the data. The diffraction patterns were then indexed, and the lattice parameters obtained by Rietveld refinement.

Thermal analysis.—The thermal behaviors of the prepared samples were monitored with a Perkin-Elmer 7 Series thermal analysis system. Thermogravimetric analysis (TGA) was conducted in an artificial atmosphere of air from room temperature to 850 or 900°C with heating and cooling rates of 1.0°C/min. Thermal mechanical analysis (TMA), including the TEC, and differential temperature analysis (DTA) were carried out separately in open air from room temperature to 850°C and room temperature to 1150°C, respectively, with a heating rate of 10°C/min.

Electrical conductivity.—The conductivity of sintered samples was measured with the standard dc four-point method described by van der Pauw.[23] The sintered pellets were cut into slices with a large length/cross section ratio. Two Pt electrodes were used for conducting current along the length, and two Pt electrodes were used for measuring voltage across the section at a certain distance. The measurements were carried out in open air from 320 to 800°C in both heating and cooling cycles. The applied current and the resulting voltage were supplied and measured with a Keithley 224 current source and a HP 3478A multimeter, respectively. A computer was used to control the furnace temperature and to communicate data from the current source and multimeter. The validity of Ohm's law was checked by measuring the conductivity at different currents.

Since the density of the polycrystalline samples has a significant effect on the conductivity, the densities of all sintered pellets prepared in this study were determined with a Micromeritics Accupyc 1330 pycnometer.

Thermoelectric power.—Seebeck coefficients of sintered pellets were measured in open air from room temperature to 700°C, both heating and cooling, with a home-made device described elsewhere.[24]

Impedance spectroscopy with prepared electrodes LSCN and LSFN.—Impedance spectroscopy of the $La_{1-x}Sr_xGa_{1-y}Mg_yO_{3-0.5(x+y)}$ (LSGM) electrolyte with LSCN and LSFN electrodes was measured with an HP4192A LF impedance analyzer from 800 to 320°C in open air. The frequencies of the measurements scan from 5 Hz to 13 MHz with an ac amplitude of 40 mV; measurements were taken at a total of 25 temperatures. The impedance spectroscopy of the well-known perovskite electrodes $La_{1-x}Sr_xCoO_{3-\delta}$ (LSCo) and $La_{1-x}Sr_xMnO_3$ (LSM) were also measured and compared with the investigated electrodes.

Results and Discussion

Crystal structure.—Typical X-ray diffraction patterns are shown in Fig. 1; the compositions $La_{0.8}Sr_{0.2}Co_{0.8}Ni_{0.2}O_{3-\delta}$ and $La_{0.7}Sr_{0.3}Fe_{0.8}Ni_{0.2}O_{3-\delta}$ were chosen as examples.

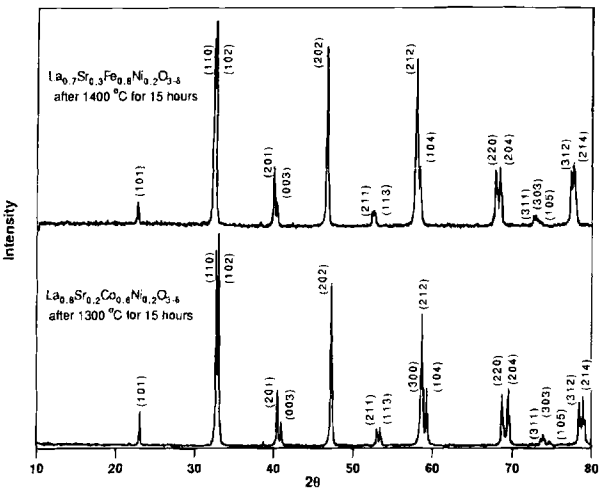

Fig. 1. Typical X-ray diffraction patterns of two optimal compositions in LSCN and LSFN systems.

The structure of the undoped perovskite $LaCoO_3$ is rhombohedral at room temperature with space group $R\bar{3}m$ (no. 166) having six formula units per unit cell. Sr and Ni doping at La and Co sites, respectively, do not change the structure of the parent perovskite, as shown in Table I (rhombohedral settings transformed from hexagonal settings), but lattice parameters do change with composition as expected. For all compositions, the a parameter is essentially invariant within experimental error. However, comparison of the distortion angles α at the same Ni doping reveals a decrease with Sr doping, which is consistent with the finding that α becomes 90° (cubic) when the Sr doping becomes $x \geq 0.5$. In contrast, at the same Sr concentration, α increases with Ni content, since Ni favors the rhombohedral structure.

All the LSCN compositions $0 \leq x \leq 0.3$, $0 \leq y \leq 0.2$ shown in Table I were found to be single phase. A small, unidentified peak at $2\theta \approx 38°$ is evident in Fig. 1 as well as in some of our studies of other perovskite systems. It does not match any component oxide; it matches the main peak of the high-pressure oxygen diffraction pattern, but we hesitate to assign it to oxygen trapped in micropores where it is put under pressure on cooling. Beyond this region, a primary impurity phase, La_2NiO_4, was found if the sintering temperature was higher than 1100°C due to the poor thermal stability of Ni^{III} in the perovskite structure. This finding agrees very well with the data of Obayashi and Kudo[10] and of Nagamoto et al.,[12] but disagrees significantly with Ftikos et al,[25] who claimed that a single cubic phase extends to $x = 0.6$ and $y = 0.4$.

The structure of $LaFeO_3$ is orthorhombic at room temperature with space group $Pnma$ (no. 62) and parameters $a = 5.5647(1)$, $b = 7.8551(1)$, and $c = 5.5560(1)$ Å [17,18] having four formula units per unit cell. At lower Sr and Ni doping levels, the perovskite structure remains orthorhombic; it changes to rhombohedral with an increase of both Sr and Ni content, as shown in Table II (rhombohedral settings transformed from hexagonal settings). Table II lists all single-phase LSFN compositions studied; they fall in the region $0 \leq x \leq 0.3$, $0 \leq y \leq 0.2$. Similar to the LSCN system, a primary unwanted impurity, La_2NiO_4, was formed outside the above compositional range. In solely Sr-doped $LaFeO_3$, the orthorhombic lattice parameters a, b, and c were found to decrease with increasing Sr content (JCPDS 35-1478). Accordingly, the orthorhombic lattice parameters a, b, and c decrease with both Sr and Ni doping, a trend also reported previously.[20] In the rhombohedral LSFN phases, unlike in the LSCN system, Sr doping at the same Ni doping increases slightly the a parameter while decreasing α; the larger Sr^{2+} favors the cubic structure. Ni doping at a given Sr doping does not alter the a parameter, but it decreases a as the smaller Ni atom, like the larger Sr^{2+} ion, increases the geometric tolerance factor.

Table I. Lattice parameters of the $La_{1-x}Sr_xCo_{1-y}Ni_yO_3$ system.[a]

	a(r), Å	α(r), degree	Ref.
$LaCoO_3$	a(h) = 5.441	$\alpha=\beta=90°$	JCPDS
(S.G.= $R\bar{3}m$, z = 6)	c(h) = 13.088	$\gamma = 120°$	25-1000
$LaCo_{0.6}Ni_{0.4}O_{3-\delta}$	3.839(5)	90.75	This work
$LaCo_{0.4}Ni_{0.6}O_{3-\delta}$	3.839(5)	90.72	This work
$La_{0.9}Sr_{0.1}Co_{0.9}Ni_{0.1}O_{3-\delta}$	3.840(6)	90.58	This work
$La_{0.9}Sr_{0.1}Co_{0.8}Ni_{0.2}O_{3-\delta}$	3.842(6)	90.62	This work
$La_{0.8}Sr_{0.2}Co_{0.9}Ni_{0.1}O_{3-\delta}$	3.841(5)	90.49	This work
$La_{0.8}Sr_{0.2}Co_{0.8}Ni_{0.2}O_{3-\delta}$	3.843(6)	90.52	This work
$La_{0.7}Sr_{0.3}Co_{0.9}Ni_{0.1}O_{3-\delta}$	3.840(5)	90.38	This work
$LaNiO_3$	a(r) = 3.838	90.38	13
(S.G. = $R\bar{3}m$, z = 1)			

[a] a(r): rhombohedral lattice parameter; a(h) and c(h) are hexagonal parameters.

Thermal analysis.—Figure 2 shows DTA and TGA curves of composition $La_{0.8}Sr_{0.2}Co_{0.8}Ni_{0.2}O_{3-\delta}$ measured in a mixture of 21%O_2 + 79%N_2. The DTA curves of Fig. 2a showed only a broad endothermic peak starting from about 700°C on heating; it is related to the onset temperature near 650°C of oxygen loss shown in the TGA curve of Fig. 2b. The material is thermally stable up to 1150°C; 20 mol % Ni doping does not deteriorate the thermal stability of the Sr-doped $LaCoO_3$ system. The TGA curve indicates a reversible oxygen loss and gain during the heating and cooling cycles.

The DTA and TGA curves of composition $La_{0.7}Sr_{0.3}Fe_{0.8}Ni_{0.2}O_{3-\delta}$ are shown in Fig. 3a and b, where two successive runs are shown. It is very clear that an extra endothermic peak at around 180°C followed by two exothermic peaks at 300 and 340°C, respectively, are observed for the first run, but not in an immediately following second run. Obayashi and Kudo[10] pointed out a similar peak at 335°C in the DTA curve of pure $LaNiO_3$ and attributed it to oxidation of the $MO_{3-\delta}$ array, but the TGA data do not support this speculation in our case. The TGA curves, Fig. 3b, indicate a corresponding weight loss at 180°C for the first run, but no weight loss at this temperature for the immediately following second run. This observation definitely implies a desorption of adsorbed species

Table II. Lattice parameters of $La_{1-x}Sr_xFe_{1-y}Ni_yO_3$ system.

	a, b (Å)	c (Å)	Angles (°)	Ref.
$LaFeO_3$	5.5647(1)	5.5560(1)	$\alpha = \beta = \gamma = 90°$	17, 18
(S.G. = $Pnma$, z = 4)	7.8551(1)			
$La_{0.9}Sr_{0.1}Fe_{0.9}Ni_{0.1}O_{3-\delta}$	5.556(1)	5.531(1)	$\alpha = \beta = \gamma = 90°$	This work
	7.827(1)			
$La_{0.9}Sr_{0.1}Fe_{0.8}Ni_{0.2}O_{3-\delta}$	5.548(3)	5.506(2)	$\alpha = \beta = \gamma = 90°$	This work
	7.802(1)			
$La_{0.8}Sr_{0.2}Fe_{0.9}Ni_{0.1}O_{3-\delta}$	5.534(2)	5.509(1)	$\alpha = \beta = \gamma = 90°$	This work
	7.822(2)			
$La_{0.8}Sr_{0.2}Fe_{0.8}Ni_{0.2}O_{3-\delta}$	a(r) = 3.897(5)	—	90.47	This work
$La_{0.7}Sr_{0.3}Fe_{0.9}Ni_{0.1}O_{3-\delta}$	a(r) = 3.900(5)	—	90.42	This work
$La_{0.7}Sr_{0.3}Fe_{0.8}Ni_{0.2}O_{3-\delta}$	a(r) = 3.900(5)	—	90.37	This work
$LaFe_{0.4}Ni_{0.6}O_{3-\delta}$	a(r) = 3.877(5)	—	90.64	This work

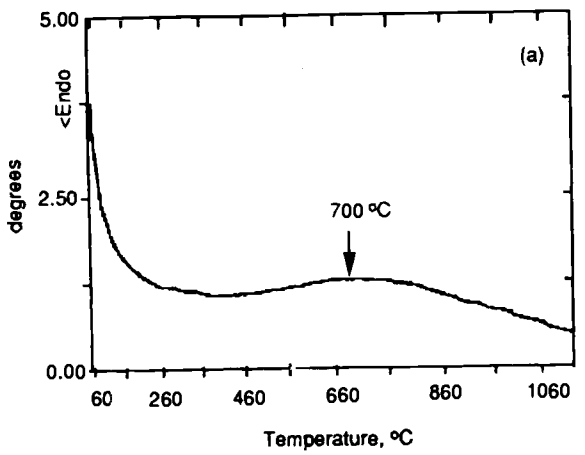

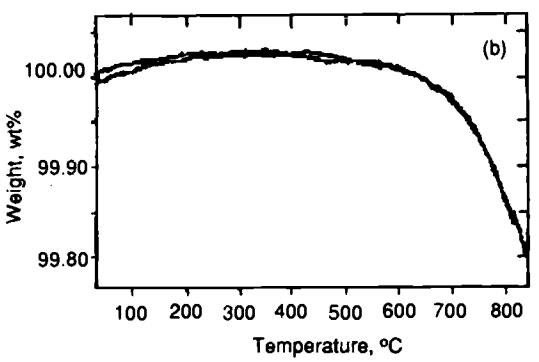

Fig. 2. (a) DTA and (b) TGA curves of $La_{0.8}Sr_{0.2}Co_{0.8}Ni_{0.2}O_{3-\delta}$.

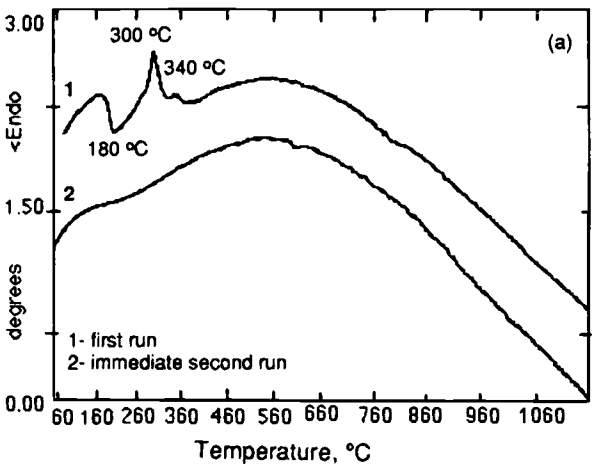

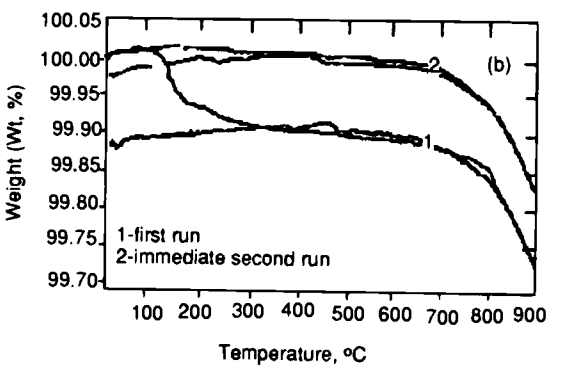

Fig. 3. (a) DTA and (b) TGA curves of $La_{0.7}Sr_{0.3}Fe_{0.8}Ni_{0.2}O_{3-\delta}$.

that are formed via a slow reaction with the atmosphere at room temperature. Since the phenomenon appears to be related to the Ni atoms, we assume that the adsorption process is associated with a reduction of Ni^{3+} to Ni^{2+} by an exchange of H_2O for $1/2O_2$, for instance, to form $Ni(OH)_2$. The exothermic peaks at 300 and 340°C do not show any weight change, which implies that an internal oxidation-reduction reaction is occurring. We postulate this to be the $Fe^{4+} + Ni^{2+} \rightleftarrows Fe^{3+} + Ni^{III}$ reaction. A broad endothermic peak starting around 700°C appears to reflect the oxygen loss that sets in close to this temperature in the TGA curve.

The TECs of all compositions investigated in this study are summarized in Table III. Compared with undoped $LaCoO_3$ and Sr- and Fe-doped $LaCoO_3$,[26,27] the Sr- and Ni-doped $LaCoO_3$ system has a lower TEC. The Sr- and Ni-doped $LaFeO_3$ system has a TEC similar to that of the electrolytes $La_{1-x}Sr_xGa_{1-y}Mg_yO_{3-0.5(x+y)}$ (LSGM) and $Zr_{1-x}Y_xO_{2-0.5x}$ (YSZ), which is a necessary requirement for the cathode of a practical SOFC. We demonstrate that LSFN also has better electrochemical properties than the cathode material $La_{1-x}Sr_xMnO_3$ (LSM), which makes it a very promising candidate to replace LSM as a cathode material in SOFCs.

Electrical properties.—Figure 4 presents the temperature dependence of the electrical conductivity $\sigma(T)$ for seven polycrystalline samples of the system $La_{1-x}Sr_xCo_{1-y}Ni_yO_3$. These $\sigma(T)$ curves are typical of a bad metal or semimetal, as reported for the $La_{1-x}Sr_xCoO_{3-\delta}$ system by others.[8,14,15] Nominal $LaCoO_3$ is a polaronic conductor at low temperatures,[28,29] but it becomes a metal at high temperatures.[16,30] The other end member, $LaNiO_3$, is metallic at all temperatures.[30] However, since the periodic potential at both the Ni and Co atoms of a $Co_{1-y}Ni_yO_3$ array is strongly perturbed by the presence of the other ions, we could expect to find polaronic conduction or a variable-range hopping with charge carriers moving primarily on a like-cation array in a pathway requiring the least energy.[31]

Polaronic conductivity is usually described by

$$\sigma = \frac{A}{T}\exp\left(-\frac{E_a}{kT}\right) \qquad [3]$$

where k is the Boltzmann factor and T is the absolute temperature. The pre-exponential factor A is proportional to $c(1-c)$, where c is the fraction of mobile charge carriers on a set of like transition-metal atoms that are mixed-valent. E_a is the activation energy for hopping of the small polarons. The corresponding Arrhenius plots of $\log(\sigma T)$ vs.

Table III. Thermal expansion coefficients α, of the studied compositions.

Compositions	Temperature range (°C)	α, x 10^6/K	Ref.
$LaCoO_3$	0–1100	22.0	11
$LaCo_{0.6}Ni_{0.4}O_{3-\delta}$	20–850	15.9	This study
$LaCo_{0.4}Ni_{0.6}O_{3-\delta}$	20–850	14.3	This study
$La_{0.9}Sr_{0.1}Co_{0.9}Ni_{0.1}O_{3-\delta}$	20–850	17.6	This study
$La_{0.9}Sr_{0.1}Co_{0.8}Ni_{0.2}O_{3-\delta}$	20–850	16.1	This study
$La_{0.8}Sr_{0.2}Co_{0.9}Ni_{0.1}O_{3-\delta}$	20–850	16.1	This study
$La_{0.8}Sr_{0.2}Co_{0.8}Ni_{0.2}O_{3-\delta}$	20–850	15.6	This study
$La_{0.7}Sr_{0.3}Co_{0.9}Ni_{0.1}O_{3-\delta}$	20–850	16.3	This study
$LaFe_{0.4}Ni_{0.6}O_{3-\delta}$	20–850	11.6	This study
$La_{0.9}Sr_{0.1}Fe_{0.9}Ni_{0.1}O_{3-\delta}$	20–850	11.7	This study
$La_{0.9}Sr_{0.1}Fe_{0.8}Ni_{0.2}O_{3-\delta}$	20–850	12.6	This study
$La_{0.8}Sr_{0.2}Fe_{0.9}Ni_{0.1}O_{3-\delta}$	20–850	12.3	This study
$La_{0.8}Sr_{0.2}Fe_{0.8}Ni_{0.2}O_{3-\delta}$	20–850	12.8	This study
$La_{0.7}Sr_{0.3}Fe_{0.9}Ni_{0.1}O_{3-\delta}$	20–850	12.4	This study
$La_{0.7}Sr_{0.3}Fe_{0.8}Ni_{0.2}O_{3-\delta}$	20–850	12.7	This study
$LaNiO_3$	0–1100	10.0	11

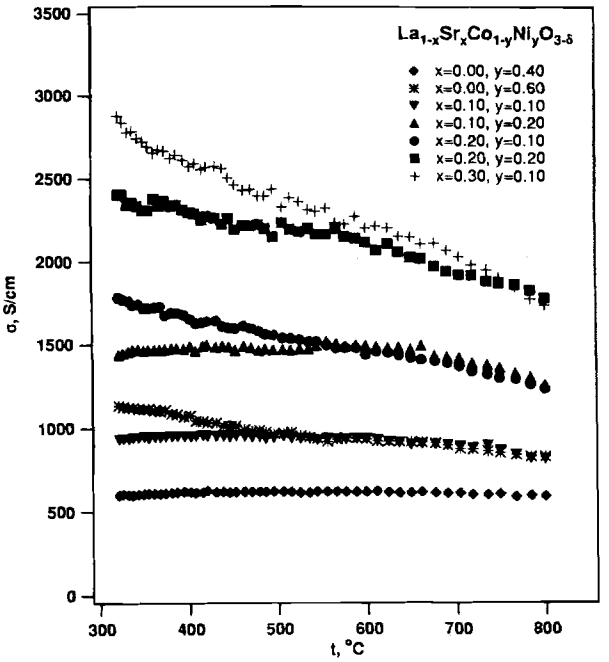

Fig. 4. Temperature dependence of conductivity for the $La_{1-x}Sr_x$-$Co_{1-y}Ni_yO_{3-\delta}$ system.

$1/T$ for the seven samples are shown in Fig. 5. Curve-fittings below 600°C yield activation energies in the range $0.02 < E_a < 0.07$ eV (see Table IV). With such low activation energies in polycrystalline samples, it is unclear to what extent they reflect grain-boundary as against intragrain conduction; therefore, the densities of the measured samples are also shown in Table IV.

Interpretation of these data as representative of intragrain conduction begins with the observation that the oxygen content does not vary below 600°C. Therefore, we assume that the oxygen content is essentially stoichiometric over the temperature range in which E_a was obtained from Eq. 3. We also note that the substitution of Sr^{2+} for La^{3+} in $La_{1-x}Sr_xCoO_{3-\delta}$ stabilizes the metallic, intermediate-spin state on the CoO_3 array;[8] thus we make the additional assumption that, above room temperature, the

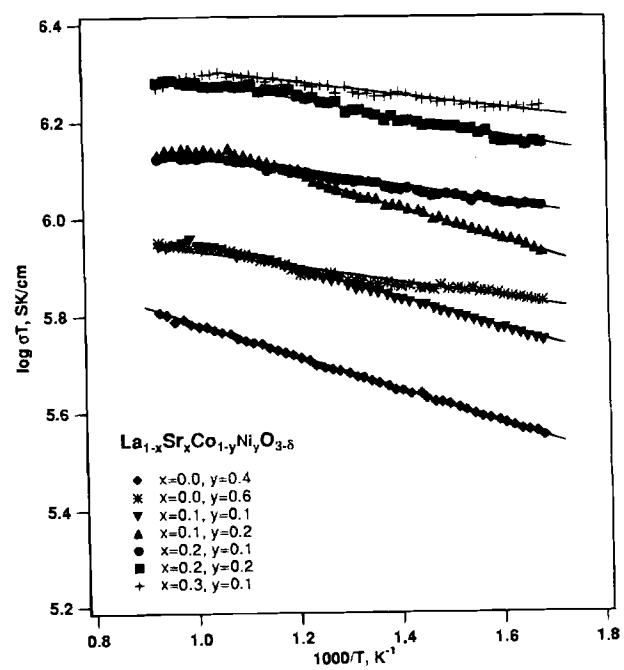

Fig. 5. Plots of log σT vs. $1/T$ for the $La_{1-x}Sr_xCo_{1-y}Ni_yO_{3-\delta}$ system.

Table IV. Activation energy of $La_{1-x}Sr_xCo_{1-y}Ni_yO_{3-\delta}$ system.

x	y	Temperature range (°C)	E_a (eV)	ρ/ρ_{th}[a]
0	0.4	320–800	0.07	0.91
0	0.6	320–800	0.03	0.97
0.10	0.10	320–700	0.06	0.95
0.10	0.20	320–700	0.06	0.92
0.20	0.10	320–700	0.05	0.91
0.20	0.20	320–700	0.04	0.89
0.30	0.10	320–700	0.02	0.84

[a] Note: ρ_{th} is the theoretical density, ρ is the sample density.

cobalt atoms are present as intermediate-spin Co^{iii} and low-spin Co^{IV} in the samples of Fig. 4 and 5.

We begin with the $x = 0$ samples, which might be expected to be single valent with only low-spin Ni^{III} and intermediate-spin Co^{iii} ions. However, the Co^{IV}/Co^{iii} redox energy lies only a little below the Ni^{III}/Ni^{2+} redox energy, and spreading of the energy ranges of each redox couple by perturbations of the periodic site potential and entropy considerations may produce some overlap of the couples. Therefore, it is necessary to consider the equilibrium reaction

$$Co^{iii} + Ni^{III} \rightleftarrows Co^{IV} + Ni^{2+} \quad [4]$$

corresponding to the charge transfer

$$t^5e^1 + t^6e^1 \rightleftarrows t^5e^0 + t^6e^2 \quad [4a]$$

The more this reaction is shifted to the right, the larger the fraction c of the mobile charge carriers on the cobalt and the nickel arrays. For $y > 0.5$, the nickel pathways are more numerous than the cobalt pathways; for $y < 0.5$ the cobalt pathways are more numerous than nickel pathways. The data of Table IV show a difference of 0.04 eV between the E_a for $y = 0.4$ and $y = 0.6$, which suggests that positive polarons on the cobalt array have a larger motional enthalpy ΔH_m, and hence a lower mobility, than the electrons in the nickel array.

Substitution of Sr^{2+} for La^{3+} on the A sites creates an equal number of Co^{IV} ions, which tends to shift reaction 4 to the left. Moreover, the Ni-atom pathways do not percolate through the lattice for $y = 0.1$; they begin to percolate only near $y = 0.2$; therefore, hole conduction on the cobalt array dominates for $0.1 \leq x \leq 0.3$ and $y < 0.2$. However, the Sr^{2+} ions have a negative lattice charge and trap Co^{IV} ions by an energy ΔH_t while repelling Ni^{2+} ions. Percolation pathways for holes trapped at Sr^{2+} ions set in near $x = 0.20$.[8] Therefore, $E_a = \Delta H_m + (1/2)\Delta H_t$ for the $x = 0.1$ samples, whereas $E_a \approx \Delta H_m$ for the Co^{IV}-polaron mobility in the $x = 0.3$ sample. It follows from Table IV that $\Delta H_m \approx 0.02$ eV and $\Delta H_t \approx 0.08$ eV for positive polarons on the cobalt array. The small increase in E_a with increasing y for fixed $x = 0.1$ or 0.2 is associated with a large increase in the conductivity. An increase in nickel concentration would increase the number of untrapped holes created by reaction 4 and introduce percolation pathways for the Ni^{2+} ions. The small change in the activation energy reflects a domination of the hole conduction.

Above 600°C, the loss of oxygen not only reduces the transition-metal cations, it also introduces mobile oxygen vacancies. An oxygen vacancy has a positive lattice charge; it therefore traps Ni^{2+} ions and repels Co^{IV} ions. Consequently, ΔH_m for the holes on the cobalt array remains essentially unchanged by the introduction of oxygen vacancies, but a progressive reduction in the density of Co^{IV} ions with increasing oxygen loss flattens the $\log(\sigma T)$ vs. $1/T$ curve for $T > 600$°C in samples where hole conduction dominates. Where negative polarons on the nickel array dominate the conductivity, as we predicted should be the case for the $x = 0$ with $y = 0.6$ sample, the extra Ni^{2+} ions added by the oxygen vacancies are trapped by the vacancy and only move with the vacancy, which has a much larger ΔH_m. Therefore, neither the concentration nor

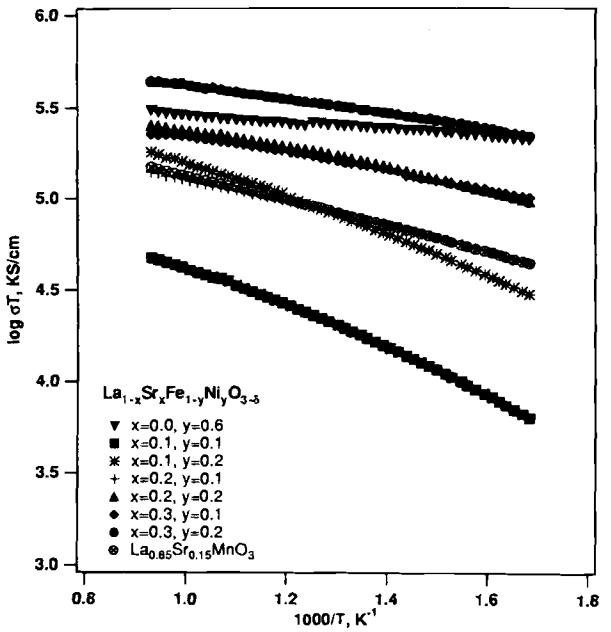

Fig. 6. Plots of log σT vs. $1/T$ for the $La_{1-x}Sr_xFe_{1-y}Ni_yO_{3-\delta}$ system.

the mobility of the fast negative charge carriers is altered appreciably by the introduction of oxygen vacancies, which is consistent with the observation that this compound shows no change of slope of the log(σT) vs. $1/T$ curve above 600°C.

Since the electrical conductivity of the system $La_{1-x}Sr_xFeO_3$ is polaronic,[29,32] Eq. 3 should apply to the $La_{1-x}Sr_xFe_{1-y}Ni_yO_3$ samples prepared in this study. The Arrhenius plots for these samples are compared in Fig. 6 with the plot for $La_{0.85}Sr_{0.15}MnO_3$ (LSM), the conventional cathode material for an SOFC. The slight curvatures occurring for samples with lower Sr and Ni doping level in Fig. 6 are possibly the result of oxygen loss beginning above 550°C; therefore, some of the E_a values given in Table V were taken from the slopes of the curves over the temperature range $320 \leq T \leq 550$°C.

Interpretation of the data is analogous to that for the $La_{1-x}Sr_xCo_{1-y}Ni_yO_3$ samples except that reaction 4 is replaced by

$$Fe^{3+} + Ni^{III} \rightleftarrows Fe^{4+} + Ni^{2+} \qquad [5]$$

corresponding to the charge transfer

$$t^3e^2 + t^6e^1 \rightleftarrows t^3e^1 + t^6e^2 \qquad [5a]$$

Reactions 4 and 5 are both applicable because the Ni^{III}/Ni^{2+} redox energy lies between the Co^{iii}/Co^{2+} and Fe^{4+}/Fe^{3+} redox energies. The literature data for $x = 0.3$ and $y = 0$ gives $E_a = 0.29$ eV,[32] and we can anticipate a larger ΔH_m for polaronic conduction in the Fe^{4+}/Fe^{3+} array compared to that in the Co^{IV}/Co^{iii} array of $La_{1-x}Sr_xCo_{1-y}Ni_yO_{3-\delta}$. The data of Table V suggest a $\Delta H_m \approx 0.1$ eV and a $\Delta H_t \approx 0.4$ eV for the Fe^{4+}/Fe^{3+} couple; a $\Delta H_m \approx 0.04$ eV for the Ni^{III}/Ni^{2+} couple compared to 0.03 eV in LSCN. A greater electron localization can be expected to make Jahn–Teller electron coupling to a local site deformation stronger at high-spin Fe^{4+} than at low-spin Ni^{III}. The large increase in $\sigma(T)$ on increasing y from 0.1 to 0.2 and x from 0.1 to 0.3 signals the introduction at $y = 0.2$ and $x = 0.2$ of percolation pathways for Ni^{2+} and Fe^{4+} conduction, respectively. Percolation pathways decrease the trapping energy ΔH_t and hence the activation energy E_a. This decrease is particularly marked with increasing x for a fixed value of y since the trapping energy $\Delta H_t = 0.4$ eV of Fe^{4+} by Sr^{2+} ions is large.

Table V. Activation energy of $La_{1-x}Sr_xFe_{1-y}Ni_yO_3$ system.

x	y	Temperature range (°C)	E_a (eV)	ρ/ρ_{th}[a]
0	0.6	320–800	0.04	0.96
0.10	0.10	320–550	0.28	0.80
0.10	0.20	320–550	0.24	0.93
0.20	0.10	320–550	0.14	0.95
0.20	0.20	320–550	0.13	0.94
0.30	0.10	320–800	0.10	0.92
0.30	0.20	320–800	0.08	0.91

[a] Note: ρ_{th} is the theoretical density, ρ is the sample density.

Figure 6 shows that the log $\sigma(T)$ *vs.* $1/T$ curves for $La_{0.85}Sr_{0.15}MnO_3$ and $La_{0.8}Sr_{0.2}Fe_{0.9}Ni_{0.1}O_{3-\delta}$ are nearly identical while $La_{0.7}Sr_{0.3}Fe_{0.8}Ni_{0.2}O_3$ has a much higher $\sigma(T)$. In addition, loss of oxygen above 550°C in the LSFN compounds makes them mixed electronic and oxide-ion conductors in the oxidizing atmosphere of the cathode, which makes them excellent candidate cathode materials for SOFCs.

Thermoelectric power.—Figures. 7 and 8 show the temperature dependence of the Seebeck coefficient $\alpha(T)$ from room temperature to 700°C for samples of the LSCN and LSFN systems. For small-polaron conduction and two types of charge carriers simultaneously present[33]

$$\alpha = \frac{\mu_n\alpha_n c_n + \mu_p\alpha_p c_p}{\mu_n c_n + \mu_p c_p} \qquad [6]$$

where μ_n and μ_p are the mobilities of the electron and hole carriers, respectively, and

$$\alpha_n = -\frac{k}{e}\ln\left[\frac{\beta(1-c_n)}{c_n}\right],\quad \alpha_p = \frac{k}{e}\ln\left[\frac{\beta(1-c_p)}{c_p}\right] \qquad [7]$$

The spin-degeneracy factor is $\beta = 2$ in our case, and

$$c_p = p/[M],\quad c_n = n/[Ni] \qquad [8]$$

with M = Co or Fe. Trapping of charge carriers by ΔH_{tn} and ΔH_{tp}, respectively, reduces the concentration of free charge carriers to

$$n = [Ni^{2+}]\exp\left(-\frac{\Delta H_{tn}}{2kT}\right)$$
$$p = [M^{4+}]\exp\left(-\frac{\Delta H_{tp}}{2kT}\right) \qquad [9]$$

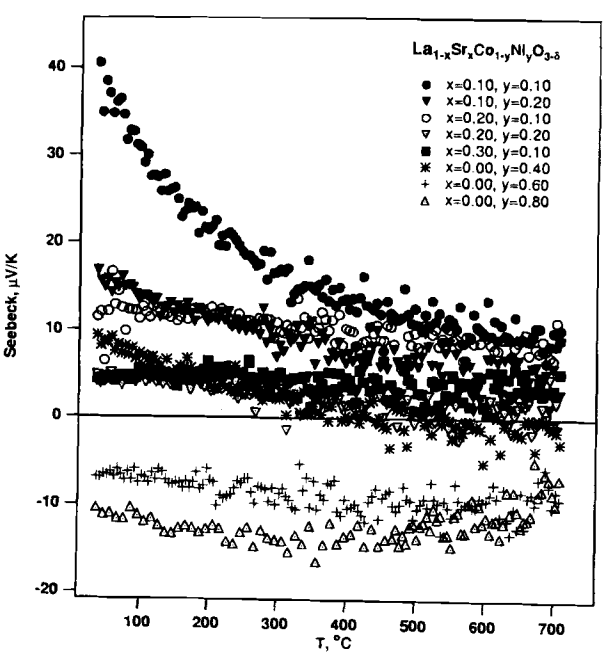

Fig. 7. Temperature dependence of the Seebeck coefficient α for the $La_{1-x}Sr_xCo_{1-y}Ni_yO_{3-\delta}$ system.

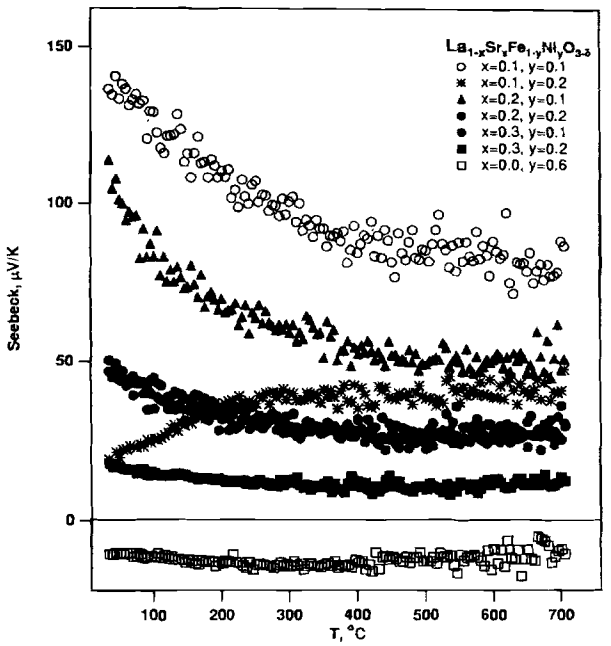

Fig. 8. Temperature dependence of the Seebeck coefficient α for the $La_{1-x}Sr_xFe_{1-y}Ni_yO_{3-\delta}$ system.

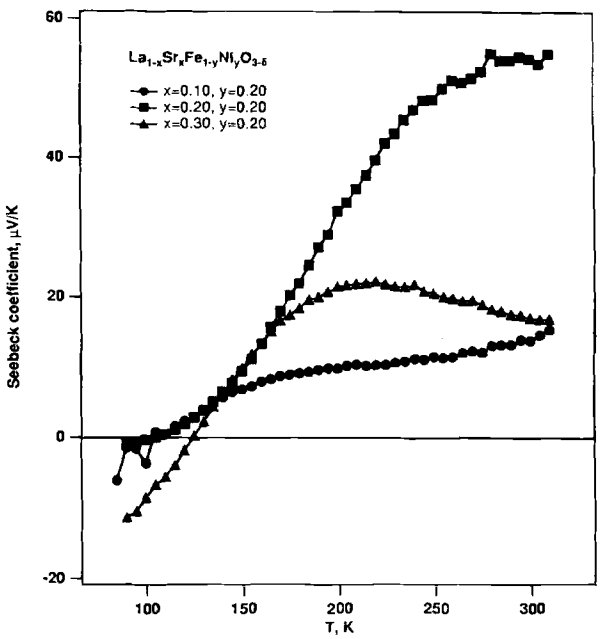

Fig. 9. Temperature dependence of Seebeck coefficient α for $La_{1-x}Sr_xFe_{1-y}Ni_yO_{3-\delta}$ system at low-temperature range, where x = 0.1, 0.2, 0.3, and y = 0.2.

This formalism allows a qualitative interpretation of Fig. 7 and 8.

According to our model of the conduction process, the $x = 0$ samples should be dominated by positive polarons for $y < 0.5$ and by negative polarons for $y > 0.5$. Accordingly, the $y = 0.6$ and 0.8 samples of Fig. 7 and 8 all show a nearly temperature-independent $\alpha < 0$ below 500°C with a decrease in $|\alpha|$ with increasing temperature $T >$ 500°C that correlates with a progressive loss of oxygen and also an anticipated increase in charge carriers via thermal excitation of reactions 4 or 5. Moreover, all the $y \leq 0.4$ samples have an $\alpha > 0$ at temperatures $T < 400$°C. Only the $x = 0$, $y = 0.4$ sample of Fig. 7 definitely shows a change of sign of α at higher temperatures. In this sample, equal numbers of electrons and holes are created by reaction 4, and percolation pathways are available to both Co^{IV} and Ni^{2+} ions. However, a greater number of pathways for Co^{IV} motion would favor p-type conduction at lower temperatures. Loss of oxygen at higher temperatures would increase the concentration of Ni^{2+} ions and decrease the concentration of Co^{IV}, which favors the change to an $\alpha < 0$.

In Fig. 7 and 8, the $x = 0.1$, $y = 0.1$ samples have the smallest concentration of mobile holes and therefore the largest α_p of a given system. Since the Ni atoms do not form percolation pathways, the negative contribution to α from α_n is minimal; therefore, $\alpha > 0$ is large and increases with decreasing temperature due to a progressive trapping of the mobile holes at the Sr^{2+} ions. Any contribution from the disproportionation reaction $2Co^{III}:t_2^5e^1 \rightleftarrows Co^{2+}:t_2^5e^2 + Co^{IV}:t_2^5e^0$ appears to be small in view of the large $\alpha > 0$ at the highest temperatures of this study. The larger magnitude of $\alpha(T)$ in Fig. 8 compared to Fig. 7 reflects the larger ΔH_{tp} in the LSFN sample. At temperatures $T > 600$°C, oxygen loss decreases the concentration of mobile holes, and $\alpha(T)$ flattens out.

Increasing y to $y = 0.2$ introduces percolation pathways for the negative polarons that are created by reactions 4 and 5; it also creates more positive polarons, which lower α_p, and $\alpha > 0$ reflects the dominance of the hole conduction at high temperatures. At low temperatures, most of the holes introduced by the Sr^{2+} ions are trapped, and α is determined by the untrapped holes and electrons created by reaction 4 or 5. Where the conduction remains dominated by the holes, an increase in α with decreasing temperature reflects trapping of the holes at Sr^{2+} ions, and this situation is found in the LSCN system of Fig. 7. In the LSFN system of Fig. 8, the negative charge carriers have a much lower motional enthalpy ΔH_m, which makes α_n competitive with α_p even above room temperature as the holes introduced by the Sr^{2+} ions are trapped.

At the lowest temperatures, holes introduced by $x = 0.1$ Sr^{2+} ions are trapped and a nearly equal number of mobile holes and electrons is generated by reaction 5. The larger number of conduction pathways for the holes might be expected to make $\mu_p\alpha_p$ dominate $\mu_n\alpha_n$, but the negative polarons have a significantly lower ΔH_m, which makes $|\mu_n\alpha_n|$ increase relative to $\mu_p\alpha_p$ as the temperature decreases. In order to determine whether $\mu_n\alpha_n$ dominates $\mu_p\alpha_p$ at lower temperatures, the $\alpha(T)$ data of Fig. 9 were taken. The $\alpha(T)$ curve becomes negative not only for $x = 0.1$ but also for 0.2 and 0.3, where fewer holes are trapped by Sr^{2+} ions because they have access to percolation pathways. Nevertheless, the relatively large motional enthalpy for the holes on the iron array allows $\mu_n\alpha_n$ to become dominant at the lowest temperatures in the $x = 0.2$ and 0.3 samples also.

Impedance spectroscopy.—Figure 10 compares two-probe impedance spectroscopy data taken in air at 800°C with LSGM as the solid electrolyte sandwiched between two like cathode materials consisting of (a) $La_{0.8}Sr_{0.2}Co_{0.8}Ni_{0.2}O_{3-\delta}$, (b) $La_{0.7}Sr_{0.3}Fe_{0.8}Ni_{0.2}O_{3-\delta}$, (c) $La_{0.6}Sr_{0.4}CoO_{3-\delta}$, and (d) $La_{0.85}Sr_{0.15}MnO_3$ (LSM). The electrode resistances, taken as $\Delta R = R_{5Hz} - R_{gb}$, are given in Table VI. ΔR for the LSCN electrode is smaller than that for the LSCo electrode. ΔR for the LSFN electrode is higher, but it is half that of the LSM electrode. Combining the impedance data with the TEC data of Table III shows that the LSCN and LSFN materials are promising replacements of LSCo and LSM cathodes in a SOFC. Confirmation of the superiority of these electrodes is awaiting results from commercial tests on prototype fuel cells.

Conclusions

The electrical conductivities of both the LSCN and LSFN systems appear to be polaronic with an overlap of the Co^{IV}/Co^{III} and Ni^{III}/Ni^{2+} couples in the former and of the Fe^{4+}/Fe^{3+} and Ni^{III}/Ni^{2+} couples in the latter. This overlap provides two types of polaronic conduction, p-type and n-type, with the p-type carriers moving on the Co- or Fe-atom array and the n-type carriers on the Ni-atom array. The motional enthalpies are estimated to be $\Delta H_m = 0.03$,

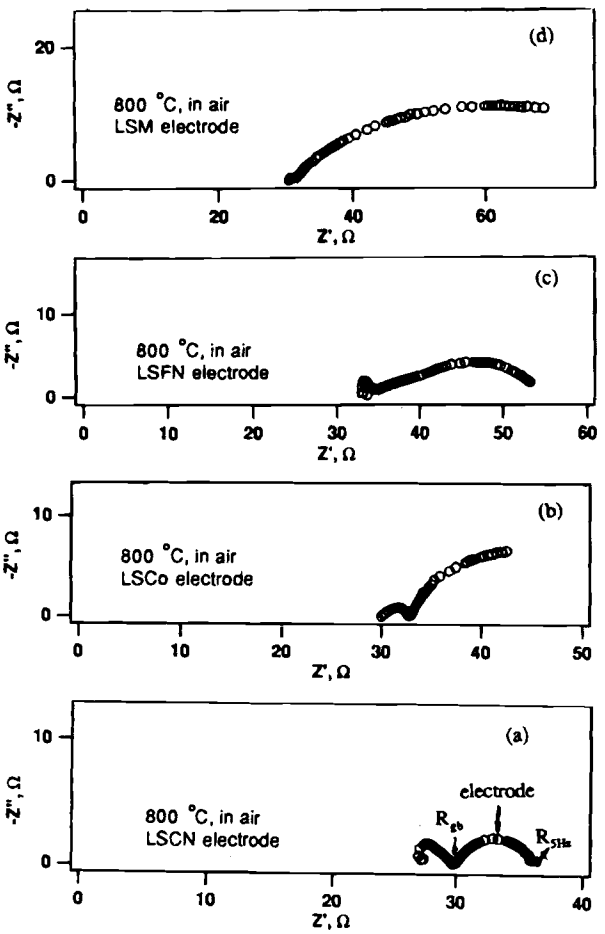

Fig. 10. Impedance spectroscopy for four types of electrodes at 800°C: LSCN, (b) LSCo, (c) LSFN, and (d) LSM.

0.02, and 0.08 eV for Ni^{2+}, Co^{IV}, and Fe^{4+} polaronic species, respectively. At lower Sr contents, the mobile holes become trapped by the Sr^{2+} ions by an energy $\Delta H_t \approx 0.08$ eV for Co^{IV} and $\Delta H_t \approx 0.4$ eV for Fe^{4+}. As a result of the larger trapping energy ΔH_t for holes in the Fe-atom array, the thermoelectric power measurements explicitly show the dominance of n-type carriers at lower temperatures with a transition from a positive to a negative effective Seebeck coefficeint on cooling. The compositions $La_{0.8}Sr_{0.2}Co_{0.8}Ni_{0.2}O_{3-\delta}$ and $La_{0.7}Sr_{0.3}Fe_{0.8}Ni_{0.2}O_{3-\delta}$ have a TEC better matched to that of electrolyte than the TEC of LSCo, and they show a comparable electrode resistance at an operating temperature $T_{op} \geq 700$°C. In contrast to the conventional $La_{1-x}Sr_xMnO_3$ cathode, these materials lose oxygen reversibly at $T >$ 600°C, which makes them mixed electronic/oxide-ion conductors with good catalytic activity for oxygen reduction. The LSCN and LSFN systems thus offer attractive alternatives to the conventional cathode materials now employed in SOFCs.

Table VI. Comparison of electrode resistance of several cathode materials at 800°C.

	R_{gb} (Ω)	R_{5Hz} (Ω)	$\Delta R = R_{5Hz} - R_{gb}$
LSCN	29.8	36.1	6.3
LSFN	34.4	53.2	18.8
LSCo	32.7	42.5	9.8
LSM	31.6	68.7	37.1

Acknowledgment

We thank EPRI (Electric Power Research Institute) for financial support under contract 8062-08. Dr. Wate T. Bakker is the manager of the project.

Manuscript submitted March 20, 1998; revised manuscript received May 13, 1998.

The University of Texas at Austin assisted in meeting the publication costs of this article.

REFERENCES

1. J. van Roosmalen, *Some Thermodynamic Properties of (La, Sr)$MnO_{3\pm\delta}$ as a Cathode Material for Solid Oxide Fuel Cells*, Netherlands Energy Research Foundation ECN, Petten, The Netherlands (1993).
2. J. H. Kuo, H. U. Anderson, and D. M. Sparlin, *J. Solid State Chem.*, **83,** 52 (1989).
3. J. H. Kuo, H. U. Anderson, and D. M. Sparlin, *J. Solid State Chem.*, **87,** 55 (1990).
4. Y. Takeda, S. Nakai, T. Kojima, R. Kanno, N. Imanishi, G. Q. Shen, O. Yamamoto, M. Mori, C. Asakawa, and T. Abe, *MRS Bull.*, **26,** 153 (1991).
5. K. Q. Huang, M. Feng, J. B. Goodenough, and C. Milliken, *J. Electrochem. Soc.*, **144,** 3650 (1997).
6. M. Feng, J. B. Goodenough, K. Huang, and C. Milliken, *J. Power Sources*, **30,** 110 (1996).
7. K. Q. Huang, R. Tichy, J. B. Goodenough, and C. Milliken, *J. Am. Ceram. Soc.*, In press (1998).
8. M. A. Señarís-Rodrígues and J. B. Goodenough, *J. Solid State Chem.*, **118,** 323 (1993).
9. J. B. Goodenough and P. M. Raccah, *J. Appl. Phys.*, **36,** 1031 (1965).
10. H. Obayashi and T. Kudo, *Jpn. J. Appl. Phys.*, **14,** 330 (1975).
11. M. Hrovat, N. Katsarakis, K. Reichman, S. Bernik, D. Kuscer, and J. Hole, *Solid State Ionics*, **83,** 99 (1996).
12. H. Nagamoto, I. Mochida, K. Kagotani, and H. Inoue, *J. Mater. Res.*, **8,** 3158 (1993).
13. H. Höfer and W. F. Kock, *J. Electrochem. Soc.*, **140,** 2889 (1993).
14. P. M. Raccah and J. B. Goodenough, *Phys. Rev.*, **155,** 932 (1967).
15. M. A. Señarís-Rodrígues and J. B. Goodenough, *J. Solid State Chem.*, **116,** 224 (1995).
16. J. B. Goodenough, *MRS Bull.*, **6,** 967 (1971).
17. D. Treves, *J. Appl. Phys.*, **36,** 1033 (1965).
18. G. R. Hearne, M. P. Pasternak, R. D. Taylor, and P. Lacorre, *Phys. Rev. B*, **51,** 11495 (1995).
19. M. Abbate, F. M. F. de Groot, J. C. Fuggle, A. Furimoto, O. Strebel, F. Lopez, M. Domke, G. Kaindl, G. A. Sawatzky, M. Takano, Y. Takeda, H. Eisaki, and S. Uchida, *Phys. Rev. B*, **46,** 4511 (1992).
20. H. Falcón and R. E. Carbonio, *J. Electroanal. Chem.*, **339,** 69 (1992); H. Falcòn, A. E. Goeta, G. Punte, and R. E. Carbonio, *Solid State Chem.*, **133,** 379 (1997).
21. R. E. Carbonio, C. Fierro, D. Tryk, D. Scherson, and E. Yeager, *J. Power Sources*, **22,** 387 (1988).
22. M. P. Pechini, U.S. Pat. 3,330,697 (1967).
23. L. J. van der Pauw, *Philips Res. Rep.*, **13,** 1-9 (1958).
24. J. B. Goodenough, J. S. Zhou, and J. Chan, *Phys. Rev. B*, **47,** 5275 (1993).
25. Ch. Ftikos, S. Carter, and B. C. H. Steele, *J. Eur. Ceram. Soc.*, **12,** 79 (1993).
26. L.-W. Tai, M. M. Nasrallah, H. U. Anderson, D. M. Sparlin, and S. R. Sehlin, *Solid State Ionics*, **76,** 259 (1995).
27. L.-W. Tai, M. M. Nasrallah, H. U. Anderson, D. M. Sparlin, and S. R. Sehlin, *Solid State Ionics*, **76,** 273 (1995).
28. R. R. Heikes, R. C. Miller, and R. Mazelsky, *Physica*, **30,** 1600 (1964).
29. J. Mizusaki, J. Tabuchi, T. Matsura, S. Yamauchi, and K. Fueki, *J. Electrochem. Soc.*, **136,** 2082 (1989).
30. J. B. Goodenough, in *Progress in Solid State Chemistry*, H. Reiss, Editor, Chap. 4, (1971).
31. G. H. Jonker, *Physica*, **20,** 1118 (1954).
32. W. H. Jung and E. Iguchi, *J. Phys.: Condens. Matter*, **7,** 1215 (1995).
33. R. G. Chamber, *Philos. Mag.*, **59,** 903 (1952).